Annals of Biomedical Engineering (© 2020)
https://doi.org/10.1007/s10439-020-02550-9

BMES BIOMEDICAL ENGINEERING SOCIETY

Original Article

Data-Driven Computational Simulation in Bone Mechanics

J. A. Sanz-Herrera,[1] J. Mora-Macías,[2] J. Ayensa-Jiménez,[3]
E. Reina-Romo,[1] M. H. Doweidar,[3] J. Domínguez,[1] and M. Doblaré[3]

[1]School of Engineering, University of Seville, Camino de los descubrimientos s/n, 41092 Seville, Spain; [2]University of Huelva, Huelva, Spain; and [3]Mechanical Engineering Department, Aragón Institute of Engineering Research (I3A), Centro de Investigación Biomédica en Red en Bioingeniería, Biomateriales y Nanomedicina (CIBER-BBN), University of Zaragoza, Zaragoza, Spain

(*Received 8 October 2019; accepted 16 June 2020*)

Associate Editor Elena S. Di Martino oversaw the review of this article.

Abstract—The data-driven approach was formally introduced in the field of computational mechanics just a few years ago, but it has gained increasing interest and application as disruptive technology in many other fields of physics and engineering. Although the fundamental bases of the method have been already settled, there are still many challenges to solve, which are often inherently linked to the problem at hand. In this paper, the data-driven methodology is applied to a particular problem in tissue biomechanics, a context where this approach is particularly suitable due to the difficulty in establishing accurate and general constitutive models, due to the intrinsic intra and inter-individual variability of the microstructure and associated mechanical properties of biological tissues. The problem addressed here corresponds to the characterization and mechanical simulation of a piece of cortical bone tissue. Cortical horse bone tissue was mechanically tested using a biaxial machine. The displacement field was obtained by means of digital image correlation and then transformed into strains by approximating the displacement derivatives in the bone virtual geometric image. These results, together with the approximated stress state, assumed as uniform in the small pieces tested, were used as input in the flowchart of the data-driven methodology to solve several numerical examples, which were compared with the corresponding classical model-based fitted solution. From these results, we conclude that the data-driven methodology is a useful tool to directly simulate problems of biomechanical interest without the imposition (model-free) of complex spatial and individually-varying constitutive laws. The presented data-driven approach recovers the natural spatial variation of the solution, resulting from the complex structure of bone tissue, i.e. heterogeneity, microstructural hierarchy and multifactorial architecture, making it possible to add the intrinsic stochasticity of biological tissues into the data set and into the numerical approach.

Address correspondence to J. A. Sanz-Herrera, School of Engineering, University of Seville, Camino de los descubrimientos s/n, 41092 Seville, Spain. Electronic mail: jsanz@us.es

Keywords—Data-driven approach, Computational biomechanics, Experimental bone tissue mechanics, Numerical simulation.

INTRODUCTION

Data Science (DS) has impacted both industry and research in an unprecedented way in our daily lives.[23] Its objective is not only to use data to feed previously established mathematical models or to find statistical properties or correlatioanans, but to unravel hidden correlations, trends, information or even knowledge, to support decisions or, in a more advanced state, to directly make such decisions. DS has found room for development in many fields, particularly in marketing, e-commerce,[13] social sciences[1] and healthcare,[28] among a vast literature and an immense variety of examples. The recent appearance of the Internet of Things will represent a new scenario for new developments of DS with endless applications.[2]

Although not at the same level, DS methodology is also starting to be applied to mathematical modeling and simulation of physical systems. This represents a new paradigm in Predictive Physics, which works in the substitution of phenomenological laws (deduction), derived from the intelligent fitting of years of tests, by the direct 'extrapolation' (induction) of the set (model-free) of available data.[21,23] The solution obtained in this way is considered to be closer, and hence more accurate, to the actual measured data, since it is not restricted to a parametric modeling of the constitutive behavior. We name this approach as data-driven (DD) modeling.

Published online: 17 July 2020

In the context of Mechanics, DD has been developed in recent years from different perspectives. Kirchdoerfer and Ortiz[16] introduced an algorithmic data-driven scheme in Continuum Mechanics which finds the closest (optimal) stress–strain solution pair from an available dataset to the set of potential solutions. This solution is enforced to fulfill the compatibility and equilibrium equations that are introduced in this formulation as constraints in the optimization function by means of Lagrangian multipliers. This formulation has been extended to dynamics,[18] and further elaborated to account for noisy datasets from a statistical perspective.[3,17] One inconvenience of data-driven simulations is the need for a complete and accurate dataset. This is not always the case, so Ayensa-Jimenez *et al.*[4] presented a general method to consistently fill and expand (upsampling) missing, incomplete and noisy datasets. Chinesta *et al.*[15] proposed applying manifold learning techniques, in combination with a directional search strategy reminiscent to the LaTin method,[20] to reduce the dimension of the dataset, making it smoother and accelerating the optimization process.

In this paper, we focus on data-driven bone tissue mechanics. Since the role of mechanics in functional aspects and long-term adaptation of biological (hard and soft) tissues is today inarguable, during the last five decades, researchers have worked on their experimental mechanical characterization to understand their behavior in both physiological and pathological conditions.[11,33] Experimental techniques such as magnetic resonance elastography,[24] indentation,[25] uniaxial tensile tests[12] and biaxial tests,[14,32] have been some of the techniques employed to quantify their properties.

Regarding mineralized tissues such as cortical bone, it has been shown that their macroscopic mechanical properties are directly related to their microscopic architecture,[38] adapting the latter to the former in the long-term in a process known as bone remodeling.[10] Recent studies presented different correlations between changes in the mechanical response with local changes in tissue composition and microstructure. Experiments with different techniques have been carried out to obtain the elastic modulus of bone tissue[26,38] and its mineral density[8] at the microscale level. These data have been directly compared with macroscopic *in vivo* or *ex vivo* experiments[26] and with computational models.[38]

Digital Image Correlation (DIC) is an optical technique that directly provides full-field displacements and strains with microscopic resolution, being suitable for testing inhomogeneous, anisotropic and nonlinear samples, such as biological tissues. The technique consists of taking digital images during the test of a specimen and comparing its initial geometry (considered as the reference state) with the final (deformed) one. DIC is a non-invasive method that allows to perform dynamic tests, with a broad range of validity and high limits for the displacements; and is carried out with a simple preparation of the specimens. This technique has been successfully used to measure deformations in bone tissue[9,40] and offers advantages over other methods, such as nanoindentation.[26,38]

All cited works use parametric modeling to fit the constitutive behavior of the tested material. However, it has been shown repeatedly[22] that the model fitting approach is far from providing sufficiently accurate results in some regions of the experiment. Therefore, a data-driven approach may represent the actual behavior of the tissue better if a sufficient set of experimental data is available.

The aim of this study is therefore to introduce a data-driven framework in the context of bone tissue mechanics, including mechanical tissue characterization. First, mechanical testing of horse cortical bone samples is performed to get the required experimental data. These samples are bi-axially loaded and the strain field of the region of interest is recorded for different loading conditions by means of DIC. These results are then used as an input dataset in the flowchart of the data-driven methodology, serving as a surrogate material for constitutive behavior models in several numerical examples. To the best of the authors' knowledge, this is the first study specifically designed for data-driven methodology simulations in the context of biomechanics. In addition, the present study adds useful new data about the mechanical properties of the equine femur in comparison to others in the literature.[7,19,27,30]

MATERIALS AND METHODS

The two components of the data-driven approach shown in this paper are: (i) building an experimental dataset of the mechanical behavior of the cortical bone tissue, and (ii) implementing a data-driven scheme to obtain the solution to problems of interest. The methods associated to these two components of the methodology are explained in the next subsections.

Bone Tissue Data Acquisition

Sample Preparation

A piece of cortical bone from the mid diaphysis was extracted from the femur of an adult horse previously fresh frozen at − 80 °C (Fig. 1a). A plane sample, 50 × 20 × 4 mm, was obtained by milling. The long sides of the rectangular specimen are parallel to the

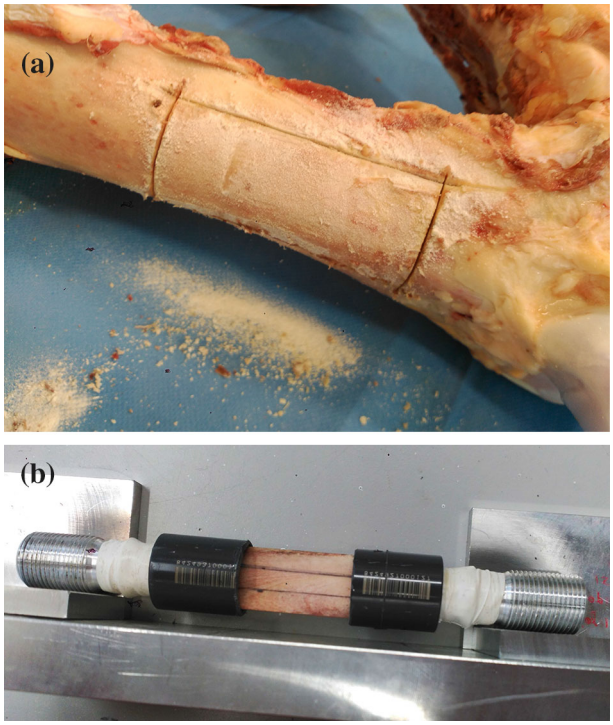

FIGURE 1. (a) Cutting process of the horse femur to extract a piece from the mid diaphysis; (b) plane sample during the embedding process.

longitudinal axis of the femur. Due to limited availability of cortical tissue, only one specimen sample was prepared for testing. The ends of the specimen, 10 mm in size, were embedded in epoxy resin to fix them to the testing machine (Fig. 1b). Once embedded, for measuring strains with the DIC technology, the sample was spray painted first to generate a white background, while little black speckles were sprayed afterwards. Fig. 2 shows the surface of the samples after painting.

Mechanical Testing

In the mechanical tests, longitudinal compressive (LF) and transversal compressive (TF) forces were applied biaxially to the sample according to the scheme shown in Fig. 2. A push-pull testing machine (KEELAVITE®) was used to apply the LF by means of an automatically controlled hydraulic actuator (MTS 407®). This system was equipped with an Eaton Lebow 20 Klbf load cell (model: 3174-20K) for LF measurement. As observed in Fig. 1, the sample was threaded longitudinally to the testing machine actuator. In the transversal direction, a manually controlled linear screw type actuator[41] was used to apply the TF as shown in Fig. 2. The TF was applied as a contact force between the sample lateral surface and a thick steel platen (20 × 20 × 5 mm). The platen (Fig. 2) is guided by a rectangular slider. Parallel planar surfaces

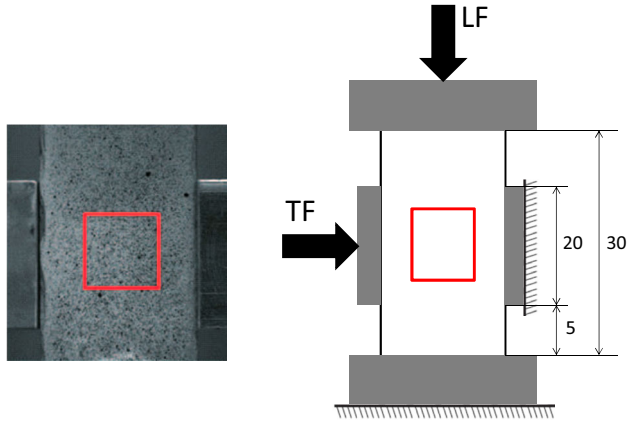

FIGURE 2. Picture of the sample taken by the DIC camera and scheme of the longitudinal forces (LF) and transversal forces (TF) applied to the specimen. The region of interest is marked in red.

of the sample, machined by milling, and appropriate tolerances between the platen and the slider, ensure uniform contact between platen and the sample surface. The TF applied, up to 1500 N, was monitored with a load cell connected in series (Interface 2 Klbf, model: WMC-2000).

Strains were measured in the 10 × 10 mm region of interest in the middle of the sample (Fig. 2) by using a DIC system (Limess®, Vic Snap® and Vic2D®). The camera provided a 38 × 32 mm field of view in the sample (2452 × 2052 pixels, with an approximately 15 μm pixel size). From the DIC pictures, the estimated displacements in the spray-painted speckle pattern were obtained over the sample to calculate the strain field in a 10 × 10 mm region of interest (Fig. 2). The average pattern density was approximately 37 dots/mm^2. A 192 × 176 points strain field was generated in the 10 × 10 mm surface (around 733 × 667 pixels). The correlation algorithms used to estimate the displacements and strains (Vic2D) are based on gray value interpolation. Depending on the gray value, an intensity pattern is defined at each point. The intensity is a function that depends on position, displacement and strain value. Therefore, difference of intensity for the same position is due to changes in displacement and strain. The algorithm determines the displacement and strain parameters, so that the intensity values at each point in the deformed and undeformed regions match.[36,37] Among the different correlation options allowed by the software, normalized squared differences were used.

The mechanical test carried out consists of applying the LF with a triangular wave (amplitude: 1500 N, mean force value: − 750 N approximately, frequency: 0.0887 Hz) while the TF moves within the range of approximately 0 to 600 N. During loading, the DIC camera took pictures of the sample surface every 20

ms. Thus, it was possible to calculate the strain field of the region of interest for different loading states in some cycles of the triangular wave and generate a data set for the data-driven implementation. This consisted of the applied forces (LF and TF) and the mean values of the strain field in the region of interest, in the longitudinal and transversal directions (ε_L and ε_T). It was checked, by means of a finite element (FE) modeling of the experimental setup shown in Fig. 2, that both stress and strain fields are homogeneous and uniform across the measured region of interest.

Data-Driven Numerical Implementation

The implementation of the data-driven methodology proceeds by searching for the closest stress–strain pair, i.e. $(\boldsymbol{\sigma}, \boldsymbol{\varepsilon})$, in the dataset $D \equiv (\boldsymbol{\sigma}, \boldsymbol{\varepsilon})_D$, constrained to the equilibrium and compatibility equations. This may be written as follows:

$$\begin{gathered} \min_{(\boldsymbol{\sigma},\boldsymbol{\varepsilon},\boldsymbol{\sigma}_D\in D,\boldsymbol{\varepsilon}_D\in D)} \left\{\tfrac{1}{s} d^2(\boldsymbol{\sigma},\boldsymbol{\sigma}_D) + \tfrac{1}{\epsilon} d^2(\boldsymbol{\varepsilon},\boldsymbol{\varepsilon}_D)\right\} \\ s.t. \\ \nabla \cdot \boldsymbol{\sigma} = \mathbf{0} \\ \boldsymbol{\varepsilon} = \tfrac{1}{2}(\nabla \mathbf{u} + \nabla^T \mathbf{u}) \\ \boldsymbol{\sigma} \cdot \mathbf{n} = \mathbf{t}^n \quad in\ \Gamma_t \\ \mathbf{u} = \bar{\mathbf{u}} \quad in\ \Gamma_u \end{gathered} \tag{1}$$

with $\mathbf{u}$ the displacement field, s and ϵ the representative values of the stress and strain ranges in the test data, respectively; $\mathbf{t}^n$ are the prescribed values of the traction field at the Neumann boundary Γ_t, associated to the normal vector $\mathbf{n}$, while $\bar{\mathbf{u}}$ are the prescribed values of the displacement field at Dirichlet boundary Γ_u. Finally, d is the metric defining the distance of the stress–strain pair to the dataset. In this work, this metric was defined as the Euclidean distance,

$$d(\boldsymbol{x}, \boldsymbol{x}_D) = \sqrt{\sum_i (x_i - x_{i,D})^2} \tag{2}$$

Substitution of Eq. (2) into (1) yields,

$$\begin{gathered} \min_{(\boldsymbol{\sigma},\boldsymbol{\varepsilon},\boldsymbol{\sigma}_D\in D,\boldsymbol{\varepsilon}_D\in D)} \left\{\tfrac{1}{s}\|\boldsymbol{\sigma} - \boldsymbol{\sigma}_D\|^2 + \tfrac{1}{\epsilon}\|\boldsymbol{\varepsilon} - \boldsymbol{\varepsilon}_D\|^2\right\} \\ s.t. \\ \nabla \cdot \boldsymbol{\sigma} = \mathbf{0} \boldsymbol{\varepsilon} = \tfrac{1}{2}(\nabla \mathbf{u} + \nabla^T \mathbf{u}) \boldsymbol{\sigma} \cdot \mathbf{n} = \mathbf{t}^n \quad in\ \Gamma_t \mathbf{u} = \bar{\mathbf{u}} \quad in\ \Gamma_u \end{gathered} \tag{3}$$

Using a FE discretization procedure over a single element (the reader is referred to the basics of FE in Reference [42], Eq. (3) yields,

$$\begin{gathered} \min_{(\boldsymbol{\sigma}^{(e)},\boldsymbol{\varepsilon}^{(e)},\boldsymbol{\sigma}^{(e)}{}_D\in D,\boldsymbol{\varepsilon}^{(e)}{}_D\in D)} \left\{\tfrac{1}{s}\left\|\boldsymbol{\sigma}^{(e)} - \boldsymbol{\sigma}^{(e)}{}_D\right\|^2 + \tfrac{1}{\epsilon}\left\|\boldsymbol{\varepsilon}^{(e)} - \boldsymbol{\varepsilon}^{(e)}{}_D\right\|^2\right\} \\ s.t. \\ \boldsymbol{\varepsilon}^{(e)} = \mathbf{B}^{(e)} \cdot \mathbf{u}^{(e)} \\ \textstyle\sum_k w_k \cdot \mathbf{B}^{(e),T}{}_k \cdot \boldsymbol{\sigma}_k^{(e)} = \mathbf{F}^{(e)} \end{gathered} \tag{4}$$

where $\mathbf{B}^{(e)}$ is the shape function gradient matrix and $\mathbf{F}^{(e)}$ the vector of forces which accounts for the body and boundary forces. Subscript (e) denotes discretized variables defined over an element. On the other hand, w_k are the corresponding weights of the integration (Gauss) points defined over the element.

The first compatibility (discretized) constraint in (4) can be directly substituted back in the objective function. On the other hand, the second FE discretized constraint can be included via a Lagrange multiplier, finally resulting in the following expression:

$$\begin{gathered} \min_{(\boldsymbol{\sigma}^{(e)},\boldsymbol{\varepsilon}^{(e)},\boldsymbol{\sigma}^{(e)}{}_D\in D,\boldsymbol{\varepsilon}^{(e)}{}_D\in D)} \\ \left\{\tfrac{1}{s}\left\|\boldsymbol{\sigma}^{(e)} - \boldsymbol{\sigma}^{(e)}{}_D\right\|^2 + \tfrac{1}{\epsilon}\left\|\mathbf{B}^{(e)} \cdot \mathbf{u}^{(e)} - \boldsymbol{\varepsilon}^{(e)}{}_D\right\|^2 + \right. \\ \left. + \left(\textstyle\sum_k w_k \cdot \mathbf{B}^{(e),T}{}_k \cdot \boldsymbol{\sigma}_k^{(e)} - \mathbf{F}^{(e)}\right) \cdot \boldsymbol{\eta}^{(e)}\right\} \end{gathered} \tag{5}$$

Taking variations in (5), we get:

$$\delta \mathbf{u}^{(e)} = \mathbf{0} \quad \rightarrow \quad \frac{1}{\epsilon}\left(\mathbf{B}^{(e)} \cdot \mathbf{u}^{(e)} - \boldsymbol{\varepsilon}^{(e)}{}_D\right) = \mathbf{0} \tag{6a}$$

$$\delta \boldsymbol{\sigma}^{(e)} = \mathbf{0} \quad \rightarrow \quad \frac{1}{s}\left(\boldsymbol{\sigma}^{(e)} - \boldsymbol{\sigma}^{(e)}{}_D\right) + \mathbf{B}^{(e)} \cdot \boldsymbol{\eta}^{(e)} = \mathbf{0} \tag{6b}$$

$$\delta \boldsymbol{\eta}^{(e)} = \mathbf{0} \quad \rightarrow \quad \sum_k w_k \cdot \mathbf{B}_k^{(e),T} \cdot \boldsymbol{\sigma}_k^{(e)} - \mathbf{F}^{(e)} = \mathbf{0} \tag{6c}$$

Without abusing notation, s and ϵ are redefined in Eqs. (6a) and (6b).

After some algebraic manipulation of (6b) and substitution of (6c) in (6b) we obtain,

$$\begin{gathered} \sum_k w_k \cdot \mathbf{B}^{(e),T}{}_k \cdot \mathbf{B}^{(e)}{}_k \cdot \mathbf{u}^{(e)} = \sum_k w_k \cdot \mathbf{B}^{(e),T}{}_k \cdot \boldsymbol{\varepsilon}^{(e)}{}_{D,k} \\ \sum_k w_k \cdot \mathbf{B}^{(e),T}{}_k \cdot s \cdot \mathbf{B}^{(e)}{}_k \cdot \boldsymbol{\eta}^{(e)} = \sum_k w_k \cdot \mathbf{B}^{(e),T}{}_k \cdot \boldsymbol{\sigma}^{(e)}{}_{D,k} - \mathbf{F}^{(e)} \end{gathered} \tag{7}$$

Equation (7) is then integrated over all finite elements of the mesh. Hence,

$$\begin{aligned}
&\mathbb{A}_{e=1}^{N_{el}}\left(\sum_k w_k \cdot \mathbf{B}^{(e),T}{}_k \cdot \mathbf{B}_k^{(e)}\right)\cdot \mathbf{u} = \mathbb{A}_{e=1}^{N_{el}}\left(\sum_k w_k \cdot \mathbf{B}^{(e),T}{}_k \cdot \boldsymbol{\varepsilon}_{D,k}^{(e)}\right)\\
&\mathbb{A}_{e=1}^{N_{el}}\left(\sum_k w_k \cdot \mathbf{B}^{(e),T}{}_k \cdot s \cdot \mathbf{B}^{(e)}{}_k\right)\cdot \boldsymbol{\eta} = \mathbb{A}_{e=1}^{N_{el}}\left(\sum_k w_k \cdot \mathbf{B}^{(e),T}{}_k \cdot \boldsymbol{\sigma}^{(e)}{}_{D,k}\right) - \mathbf{F}
\end{aligned} \tag{8}$$

In Eq. (8), $\mathbb{A}$ is the FE assembly operator and N_{el} the number of elements of the FE mesh. Note that $\mathbf{F}$ is referred to as the global force vector after assembly.

The algorithmic implementation of the set of Eq. (8) is detailed in Box below following.[16]

In this work, the finite element and algorithmic development of box 1 was implemented using Matlab® assuming the plane stress hypothesis (using the referred FE modeling of the experimental setup shown in Fig. 2, we corroborated that the out-of-plane stress field was negligible in the region of interest).

Simulation Cases

The DD methodology is always restricted to the availability of stress–strain measurements coming from experimental setups. Due to the complexity in the 3D mechanical characterization of the bone tissue, the experimental data are restricted to the 2D case, as shown in the previous sections, as a first approach. Therefore, based on the DD finite element discretization according to the implementation described in "Data-driven Numerical implementation" section, two different simplified and academic 2D examples of application were defined.

The first application example (see Fig. 3a) refers to a square plate loaded at different longitudinal and transversal directions. Due to the simplicity of this problem, the plate was meshed using 8 triangular and linear elements. This problem was simulated using our implemented DD approach. Additionally, the analytical solution of this problem allowed us to fit a constitutive model for the tested cortical bone material, as used by others,[6,39] assuming an orthotropic behavior:

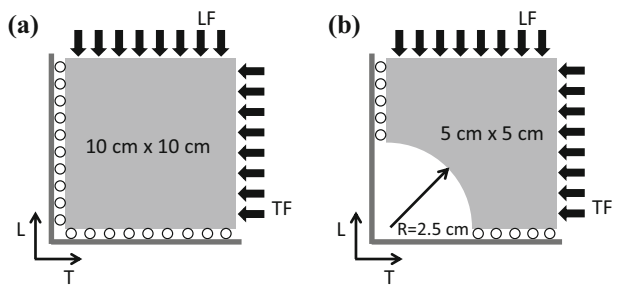

FIGURE 3. Examples of application for the data-driven simulations. (a) Square plate under biaxial compressive loading. (b) Plate with a hole under biaxial compressive loading.

$$\begin{bmatrix}\varepsilon_L\\ \varepsilon_T\end{bmatrix} = \begin{bmatrix}1/E_L & -\nu_{TL}/E_T\\ -\nu_{LT}/E_L & 1/E_T\end{bmatrix}\cdot\begin{bmatrix}\sigma_L\\ \sigma_T\end{bmatrix} \tag{9}$$

where ε_L and ε_T are the longitudinal and transversal strains, respectively; σ_L and σ_T are the longitudinal and transversal stresses, respectively; and E_L and E_T are the longitudinal and transversal Young's moduli, respectively. ν_{LT} is the Poisson's ratio in the longitudinal-transversal plane. Due to the symmetry of the compliance matrix in (9), $\nu_{TL} = \nu_{LT}E_T/E_L$. This fitting procedure is the classical alternative way of solving the problems in Figs. 3a and 3b, and allowed us to compare the DD results with the standard FE ones, as shown in "Data-Driven Results" section.

On the other hand, the example of application shown in Fig. 3b was solved for a biaxial compressive load of TF = 1.3×10^5 N/m and LF = 2.6×10^5 N/m, both using the model free DD approach and standard FE simulations together with the referred classical fitting approach, assuming an orthotropic material modeling, as shown above. The FE mesh was composed of 1024 triangular linear elements (Fig. 4). Finer meshes yielded average differences in results below 2%, such that the selected mesh was considered independent from results.

In order to quantify the differences between the model free DD and the model-based FE simulations, the following *difference* indicators were defined:

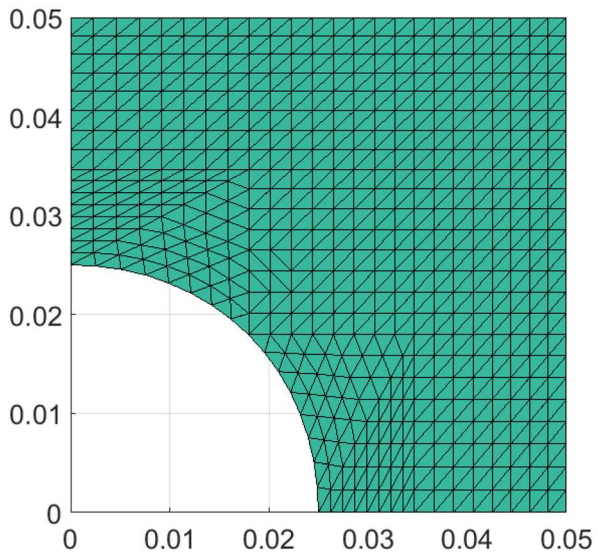

FIGURE 4. FE mesh for the application example shown in Fig. 3b.

$$
\begin{aligned}
\text{diff}(u_L^i)\ [\%] &= 100 \cdot \left\| \frac{u_L^{i,FE} - u_L^{i,DD}}{\text{mean}\left[u_L^{i,FE}\right]} \right\| \\
\text{diff}(u_T^i)\ [\%] &= 100 \cdot \left\| \frac{u_T^{i,FE} - u_T^{i,DD}}{\text{mean}\left[u_T^{i,FE}\right]} \right\| \\
\text{diff}(\varepsilon_L^i)\ [\%] &= 100 \cdot \left\| \frac{\varepsilon_L^{i,FE} - \varepsilon_L^{i,DD}}{\text{mean}\left[\varepsilon_L^{i,FE}\right]} \right\| \\
\text{diff}(\varepsilon_T^i)\ [\%] &= 100 \cdot \left\| \frac{\varepsilon_T^{i,FE} - \varepsilon_T^{i,DD}}{\text{mean}\left[\varepsilon_T^{i,FE}\right]} \right\| \\
\text{diff}(\sigma_L^i)\ [\%] &= 100 \cdot \left\| \frac{\sigma_L^{i,FE} - \sigma_L^{i,DD}}{\text{mean}\left[\sigma_L^{i,FE}\right]} \right\| \\
\text{diff}(\sigma_T^i)\ [\%] &= 100 \cdot \left\| \frac{\sigma_T^{i,FE} - \sigma_T^{i,DD}}{\text{mean}\left[\sigma_T^{i,FE}\right]} \right\|
\end{aligned}
\tag{10}
$$

with u_L^i, u_T^i, ε_L^i, ε_T^i, σ_L^i and σ_T^i the longitudinal and transversal components of the field variables, at each node i of the FE mesh, respectively. Superindexes *FE* and *DD* refer to the method with which the solution was computed. Finally, mean[•] denotes the mean value of all the nodes of the FE mesh of the corresponding input variable.

RESULTS

Bone Tissue Experimental Results

Figure 5 shows the values of the LF and TF versus time (Fig. 5a) for the time points in which strains in the region of interest were recorded using DIC, i.e. when a picture was taken by the DIC system. It is observed that the LF follows a triangular wave between 0 and − 1500 N while the TF decreases up to − 600 N (Fig. 5a). Figure 5b shows the mean values of the longitudinal (Le) and transversal (Te) strains in the region for the same time points represented in Fig. 5a. Le ranges between 0 and − 0.1%, reaching the lowest values when the transversal force is the highest. Te ranges between 0.05 and − 0.05%, with the minimum values of Te reaching the maximum TF in compression. The strain field, measured with DIC, is given in Fig. 6, for LF= −458.0 N and TF= −531.9 N. The

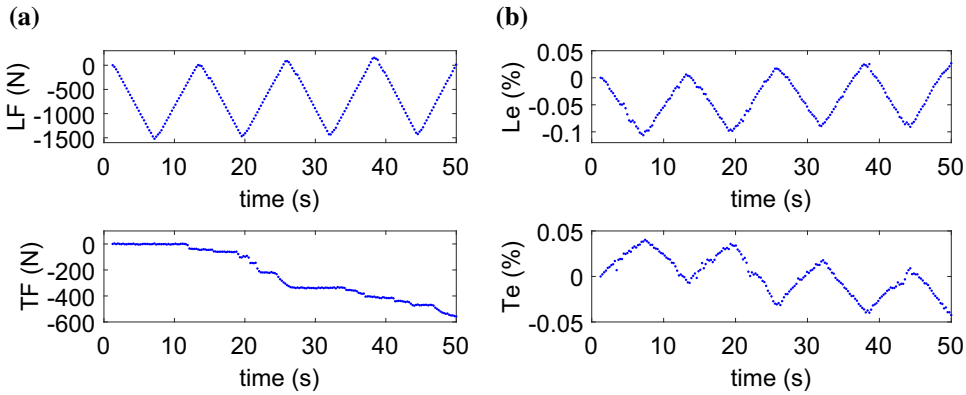

FIGURE 5. (a) Longitudinal force (LF) and transversal force (TF); (b) mean longitudinal strain (Le) and transversal strain (Te).

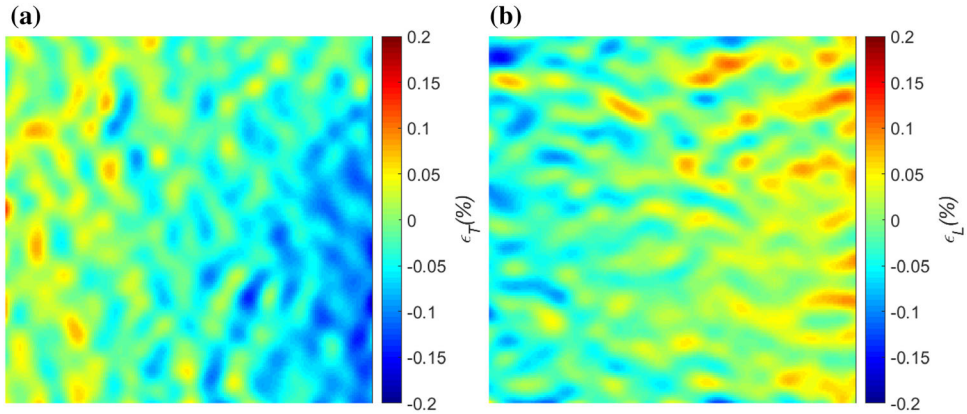

FIGURE 6. Experimentally (DIC) obtained microscopic transversal (a) and longitudinal (b) strain fields for LF= −458.0 N and TF=-531.9 N.

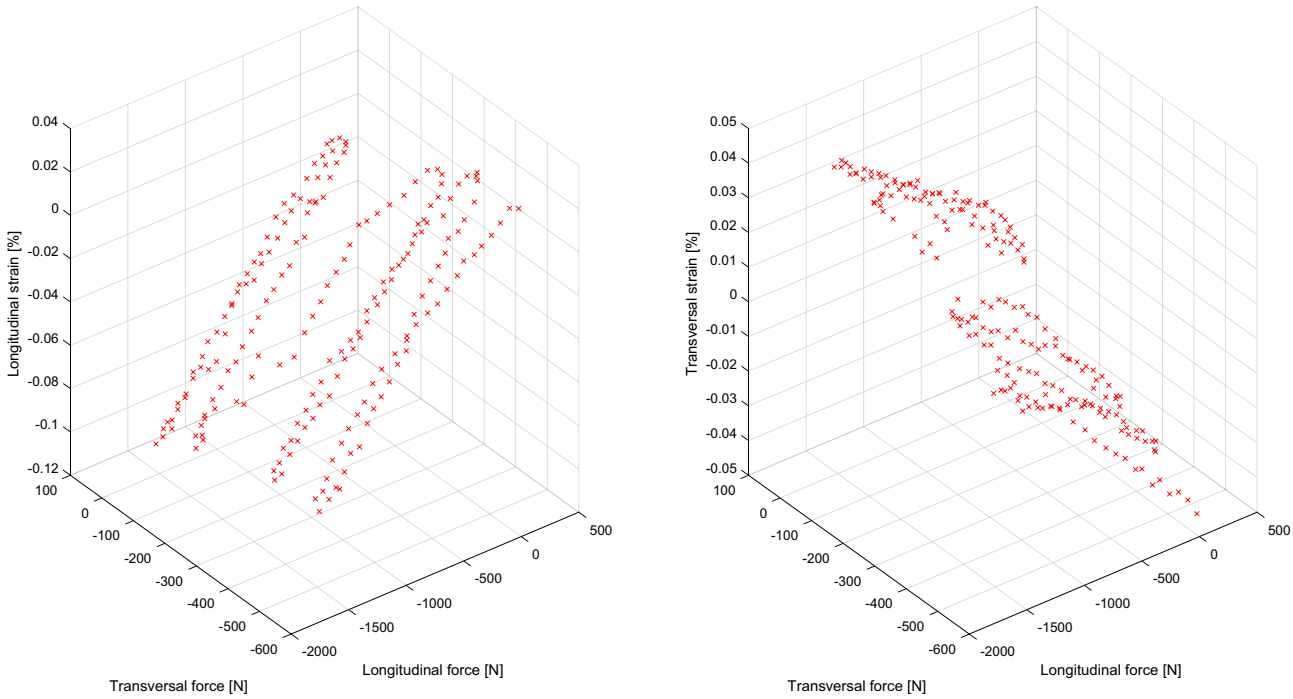

FIGURE 7. Horse femur cortical bone behavior. Measured dataset.

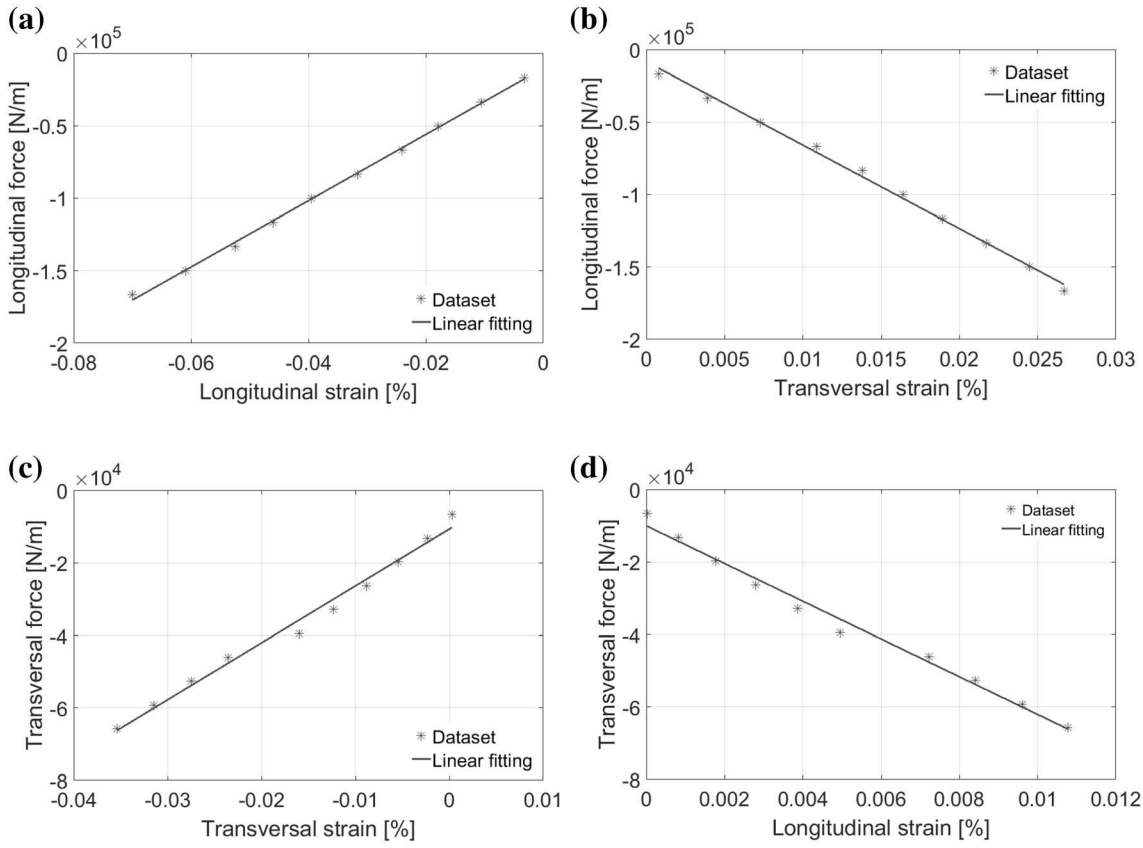

FIGURE 8. Results for the square plate subjected to longitudinal and transversal forces (Fig. 3a). Longitudinal force versus (a) longitudinal strain and (b) transversal strain for a null value of the transversal force. Transversal force versus (c) transversal strain and (d) longitudinal strain for a null value of the longitudinal force.

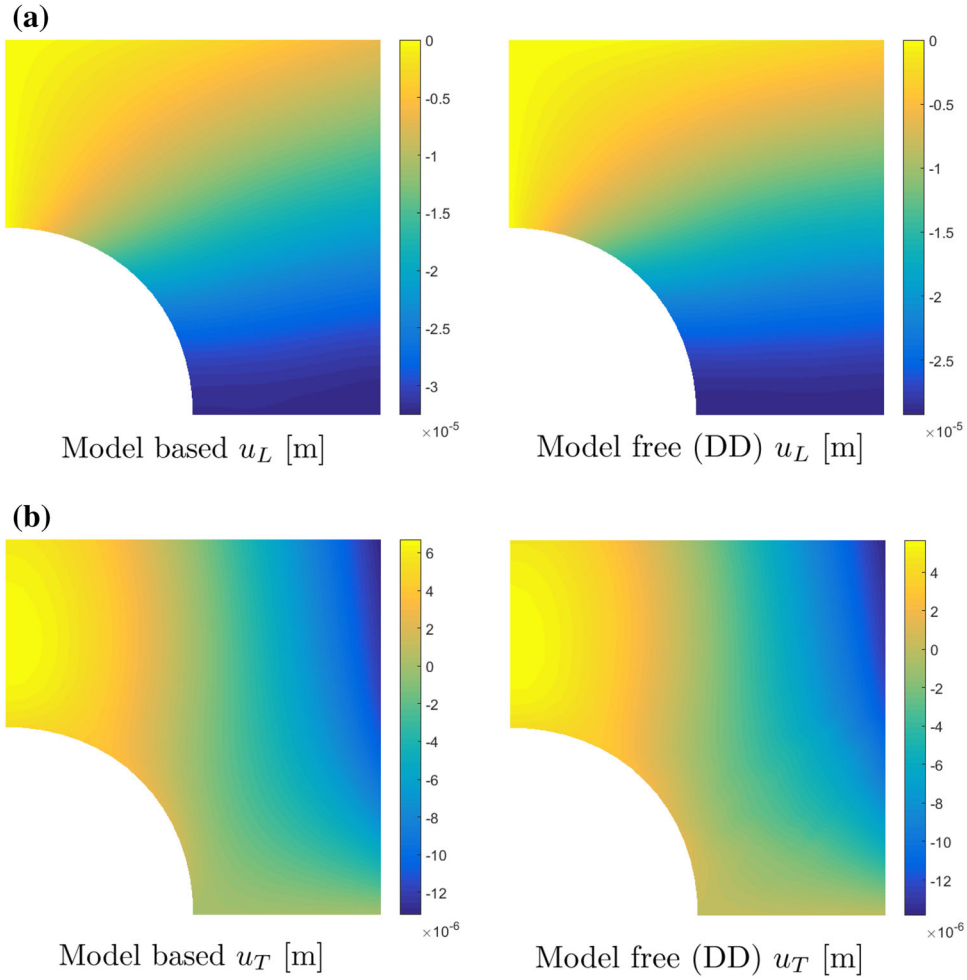

FIGURE 9. Plate with a hole under a biaxial compressive loading of TF = 1.3 × 10^5 N/m and LF = 2.6 × 10^5 N/m. Displacement field [m]. Left: Model based fitting solution. Right: DD simulations. (a) Longitudinal displacement. (b) Transversal displacement.

measured stress values, needed in the dataset for the DD simulations ("Data-driven Numerical Implementation" section), were obtained by dividing the measured forces shown in Fig. 5a by the compressive area (20 × 4 mm) in the tests (Fig. 2).

The results presented in this section for the test described in "Bone Tissue Data Acquisition" section are then model-free, used without any previous fitting or calibration procedure. Hence, the results were obtained without the need to determine the overall mechanical properties to model the cortical bone behavior. Instead, these results are used as the dataset for the data-driven simulations as described in "Data-Driven Numerical Implementation" section. This dataset is shown in Fig. 7. The results of the simulations are presented in the next section.

Data-Driven Results

The plate of the first example of application (see Fig. 3a) was first subjected to a range of transverse force with null longitudinal component. Then, the plate was subjected to a range of longitudinal forces with null transversal component. The DD simulations provided a constant stress and strain level along the plate, which is basically the closest point of solution in the dataset. The DD results of these simulations can be seen in Fig. 8 (dot plot) for the considered range of longitudinal and transversal forces. This problem allowed us to fit the constitutive model Eq. (9), using minimum square fitting, as plotted in Fig. 8 over the measured values in the dataset. The model yields the following mechanical parameters for a 2D orthotropic behavior: $E_L = 22.9\,GPa$, $E_T = 15.7\,GPa$, $v_{TL} = 0.30$ and $v_{LT} = 0.44$. These fitted mechanical properties were used in standard FE simulations for the problem shown in Fig. 3b, as is presented next.

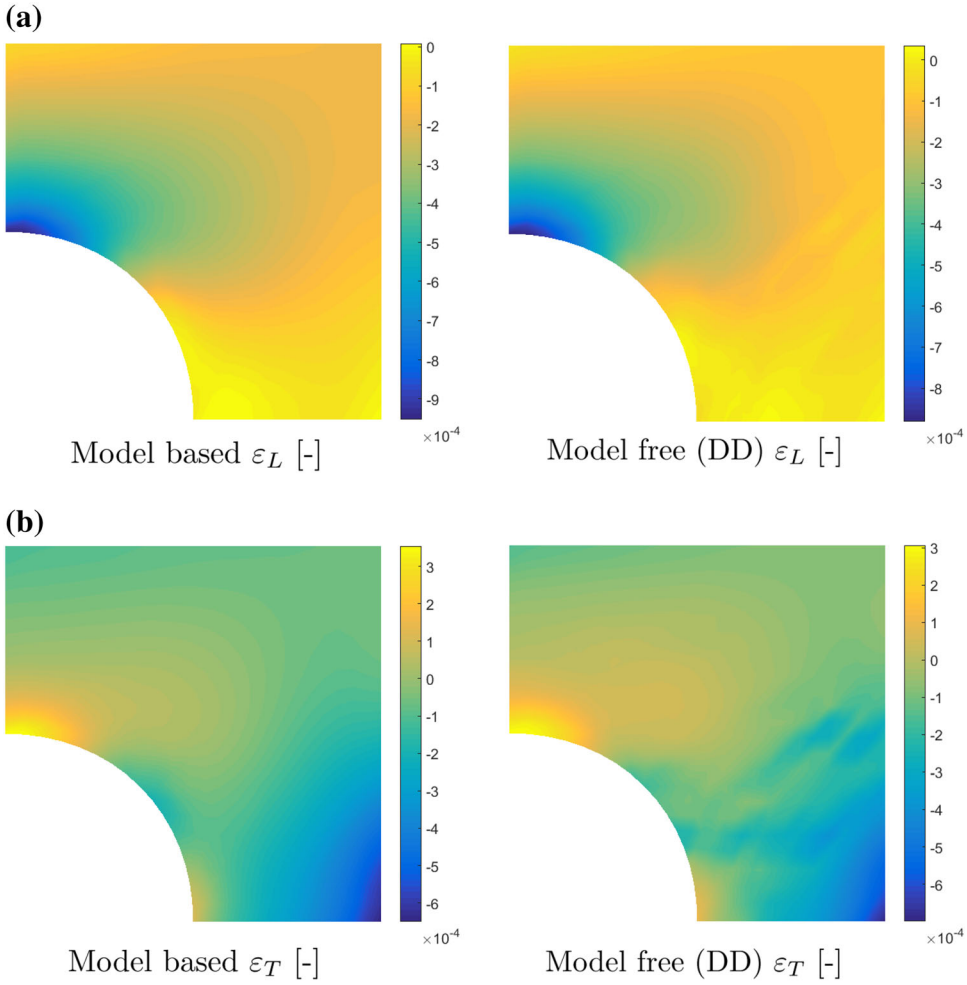

FIGURE 10. Plate with a hole under a biaxial compressive loading of TF = 1.3 × 10^5 N/m and LF = 2.6 × 10^5 N/m. Strain field [–]. Left: Model based fitting solution. Right: DD simulations. (a) Longitudinal strain component. (b) Transversal strain component.

The longitudinal and transversal components of the displacement field are shown in Fig. 9 for the DD and model-based (standard) FE simulations. Also, the longitudinal and transversal components of the strain and stress tensors are plotted in Figs. 10 and 11, respectively, for both approaches.

Finally, Fig. 12 shows the difference maps along the geometry of the plate with a hole for the different analyzed variables defined.

DISCUSSION

The results presented in this work provide, on one hand, additional data regarding the characterization of cortical bone tissue mechanics given the experimental setup implemented specifically in this study. This setup was based on the DIC technique, which proved to be very useful to properly characterize the stress–strain relation for cortical bone. In fact, a classical model-based fitting was carried out in this work, yielding the following values (considered as an orthotropic material): $E_L = 22.9\,GPa$, $E_T = 15.7\,GPa$, $\nu_{TL} = 0.30$ and $\nu_{LT} = 0.44$. This information is complementary to other studies performed on the cortical bone. For example, values in the range 15-22 GPa were reported for the elasticity modulus of equine cortical bone.[5,29,31,34] For human bone tissue, values in the range 10–25 GPa are found for the elasticity modulus, and 0.3–0.6 for the Poisson's ratio.[35]

On the other hand, and most interestingly, the orthotropic model-based fitting for the behavior of the cortical bone tissue allowed us to compare FE simulations with those obtained with the model-free DD approach proposed in this paper. Apparently, and according to Figs. 9, 10, 11, similar trends and values were obtained for the field variables following both methodologies. The displacement field is smooth both for FE and DD simulations, as shown in Fig. 9. However, it can be observed in Figs. 10 and 11 that the

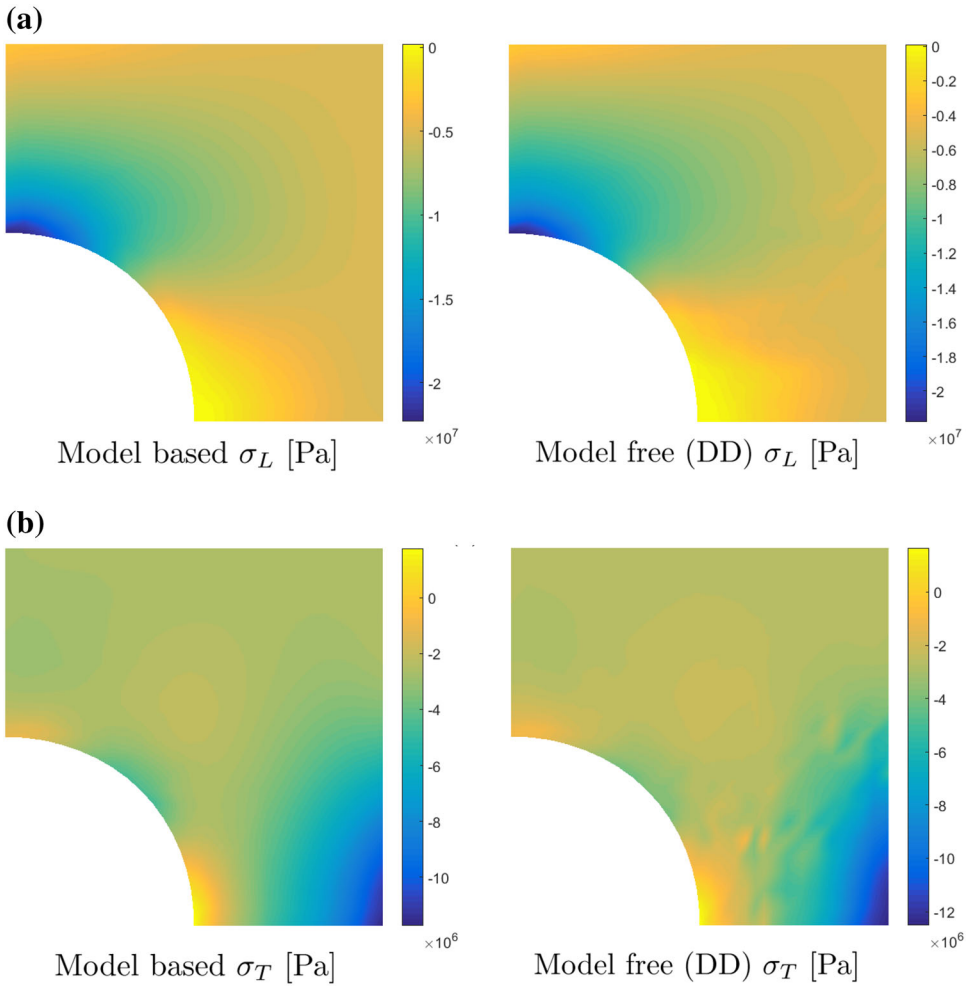

FIGURE 11. Plate with a hole under a biaxial compressive loading of TF = 1.3 × 10^5 N/m and LF = 2.6 × 10^5 N/m. Stress field [Pa]. Left: Model based fitting solution. Right: DD simulations. (a) Longitudinal stress component. (b) Transversal stress component.

fluctuation found in the results, typically obtained in the experimental tests as can be seen in the dataset in Fig. 7, is naturally recovered and reproduced for both strain and stress in the DD simulations, in contrast to the smoother solution obtained by means of the FE analysis. This fluctuation found in the tests is a direct consequence of the heterogeneity, microstructural hierarchy and multifactorial architecture of the cortical tissue, and demonstrates that model-based fitting differs from the actual behavior. In fact, indicators of the difference between the variable fields (as defined in Eq. (10)) are non-negligible in some regions of the domain, with values of the the order of 25–80% for the longitudinal and transversal components of the displacement field; of 30–70% for the longitudinal and transversal components of the strain field (peak values up to 50 and 170% at some local regions for the longitudinal and transversal components, respectively); and 14–40% for the longitudinal and transversal components of the stress field (peak values up to 60% at some local regions for the transversal component). A higher difference magnitude is repeatedly observed in the transversal direction than in the longitudinal one, according to Figs. 9, 10, 11. This may be attributed to the higher dispersion found in the experimental results in the transversal direction, as seen in Figs. 8c and 8d in comparison to the longitudinal direction (Figs. 8a and 8b).

As main limitations of this study, we can mention the different hypotheses assumed with respect to the acquisition of strains from the bone tissue and how they were post-processed. Some of these hypotheses are associated to the tissue properties. On the one hand, cortical bone tissue is a heterogeneous and not fully perfect linear elastic material. The mean value of the strains from a discrete (DIC) strain field (with approximately 57 μm among points of the speckle in average) was used as input for the data-driven imple-

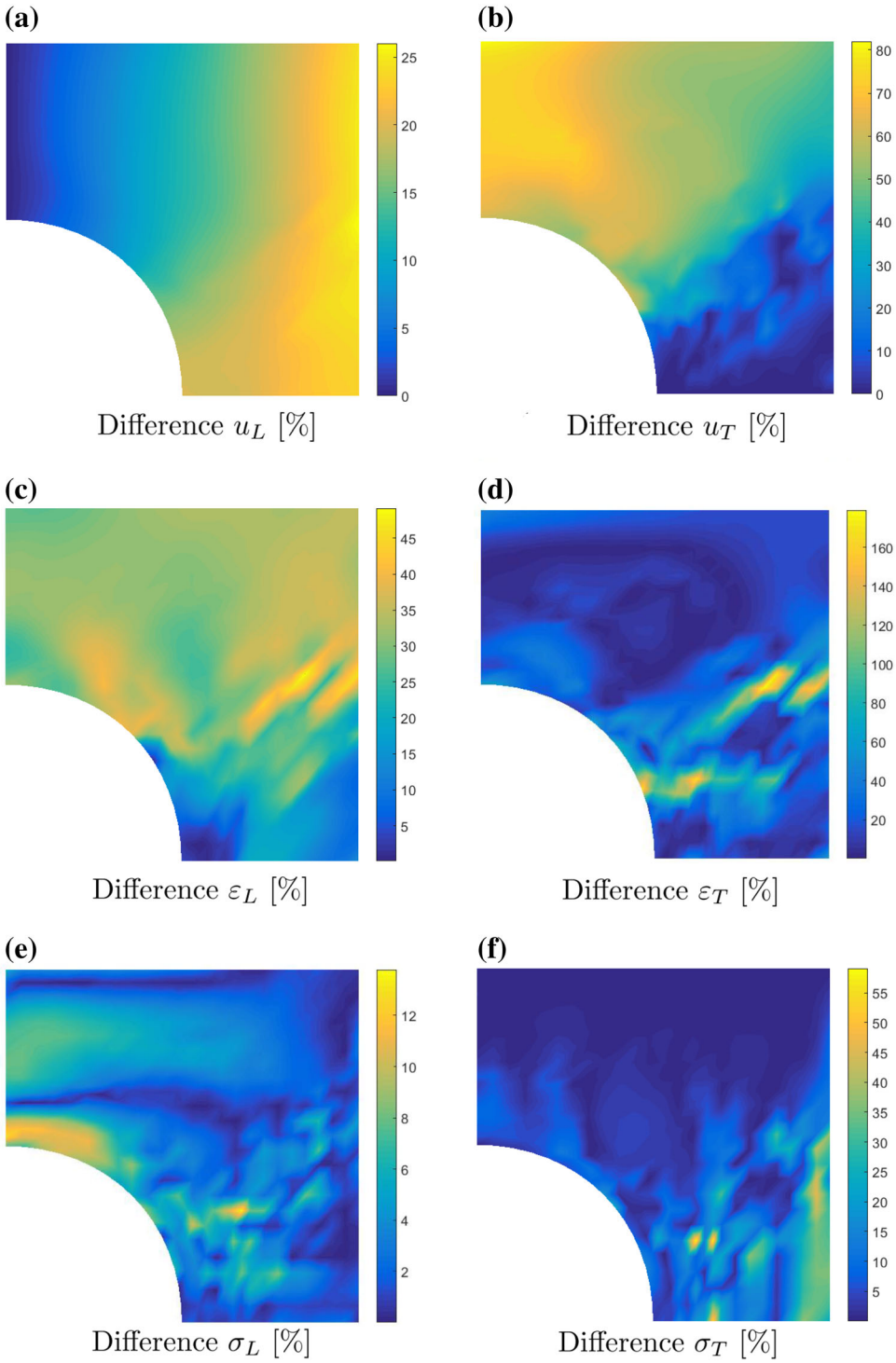

FIGURE 12. Plate with a hole under a biaxial compressive loading of TF = 1.3 × 10^5 N/m and LF = 2.6 × 10^5 N/m. Variable field difference in [%] as computed from Eq. (10). (a) diff(u_L^i), (b) diff(u_T^i), (c) diff(ε_L^i), (d) diff(ε_T^i), (e) diff(σ_L^i) and (f) diff(σ_T^i).

mentation, assuming a continuous elastic behavior. Therefore, the effect of bone heterogeneity in the mean value of strain has been considered, but not the local differences, which would require multiscale techniques. Regarding the sample preparation, the size and homogeneity of the speckle pattern was also limited, since painting was applied manually. That limits the scale of the strain measurements. On the other hand, the increase of thickness of the sample due to painting has been neglected. Finally, the main limitation of this

study was the use of a single bone sample to illustrate the methodology given the focus and scope of the present work. More samples and regions of interest within each sample would reinforce the conclusions provided by this study. This will be the focus of future work.

Conclusions

The present study shows, for the first time, the development of an experimental setup for the characterization of cortical bone tissue mechanics in connection with DD simulations. The comparison of the model-free DD methodology versus the classical constitutive modeling approach and FE simulations suggests that DD simulations are more realistic and accurate to analyze cortical bone mechanics, since they naturally recover the typical fluctuations in the stress–strain tests. We hypothesize that the fluctuations of stress and strain fields found in our DD results are a direct consequence of the heterogeneity, microstructural hierarchy and multifactorial architecture of this tissue. These preliminary results suggest that DD simulations may be an interesting alternative to be further explored, versus standard *in-silico* analysis in biomechanics.

ACKNOWLEDGMENTS

The authors gratefully acknowledge the Spanish Ministry of Economy and Competitiveness (PGC2018-097257-B-C31, DPI2017-82501-P, MAT2016-76039-C4-4-R, AEI/FEDER, UE) and Andalusian Office of Economy and Science (US-1261691, FEDER, UE) for research funding.

CONFLICT OF INTEREST

The authors declare that they have no conflict of interest.

HUMAN AND ANIMAL PARTICIPANTS

The experiment was conducted on cadaveric animal (horse) tissue. The horse femur was obtained via a butcher's service (La Pañoleta, Seville - Spain), and tested in the biomechanics research laboratory of the Department of Mechanical Engineering of the University of Seville. Then, the animal was not sacrificed for the purposes of the present study.

REFERENCES

[1]Aneshensel, C.S. Theory-based data analysis for the social sciences. Sage, 2013.
[2]Atzori, L., A. Iera, and G. Morabito. The internet of things: A survey. *Comput. Networks* 54(15):2787–2805, 2010.
[3]Ayensa-Jiménez, J., M.H. Doweidar, J.A. Sanz-Herrera, and M. Doblaré. A new reliability-based data-driven approach for noisy experimental data with physical constraints. *Comput. Methods Appl. Mech. Engrg.* 328:752–774, 2018.
[4]Ayensa-Jiménez, J., M.H. Doweidar, J.A. Sanz-Herrera, and M. Doblaré. An unsupervised data completion method for physically-based data-driven models. *Comput. Methods Appl. Mech. Engrg.* 344:120–143, 2019.
[5]Batson, E.L., G.C. Reilly, J.D. Currey, and D.S. Balderson. Post-exercise and positional variation in mechanical properties of the radius in young horses. *Equine Vet.* 32:95–100, 2000.
[6]Bernard, S., Q. Grimal, and P. Laugier. Accurate measurement of cortical bone elasticity tensor with resonant ultrasound spectroscopy. *J. Mech. Behav. Biomed. Mater.* 18:12–19, 2013.
[7]Bogers, S.H., C.W. Rogers, C.F. Bolwell, W.D. Roe, E.K. Gee, and C.W. McIlwraith. Impact of race training on volumetric bone mineral density and its spatial distribution in the distal epiphysis of the third metatarsal bone of 2-year-oldhorses. *Vet. J.* 201(3):353–358, 2014.
[8]Bouxsein, M.L., S.K. Boyd, B.A. Christiansen, R.E. Guldberg, K.J. Jepsen, and R. Muller. Guidelines for assessment of bone microstructure in rodents using micro-computed tomography. *J. Bone Miner. Res.* 25:1468–1486, 2010.
[9]Carriero, A., L. Abela, A.A. Pitsillides, and S.J. Shefelbine. Ex vivo determination of bone tissue strains for an in vivo mouse tibial loading model. *J. Biomech.* 47:2490–2497, 2014.
[10]Doblaré, M., and J.M. García. Application of an anisotropic bone-remodelling model based on a damage-repair theory to the analysis of the proximal femur before and after total hip replacement. *J. Biomech.* 34(9):1157–1170, 2001.
[11]Duck, F.A. Physical Properties of Tissues. A Comprehensive Reference Book. 6th Ed., 1990.
[12]Fung, Y.C. Biomechanics: Mechanical Properties of Living Tissues. Springer-Verlag, Berlin, 1993.
[13]Hill, S., F. Provost, and C. Volinsky. Network-based marketing: Identifying likely adopters via consumer networks. *Statist. Sci.* 256–276, 2006.
[14]Holzapfel, G.A., and H.W. Weizsäcker. Biomechanical behavior of the arterial wall and its numerical characterization. *Comput. Biol. Med.* 28: 377–392, 1998.
[15]Ibañez, R., E. Abisset-Chavanne, J.V. Aguado, D. Gonzalez, E. Cueto, and F. Chinesta. A manifold learning approach to data-driven computational elasticity and inelasticity. *Arch. Comput. Methods Eng.* 47–57, 2016.
[16]Kirchdoerfer, T., and M. Ortiz. Data-driven computational mechanics. *Comput. Methods Appl. Mech. Engrg.* 304:81–101, 2016.
[17]Kirchdoerfer, T., and M. Ortiz. Data driven computing with noisy material data sets. *Comput. Methods Appl. Mech. Engrg.* 326:622–641, 2017.

[18]Kirchdoerfer, T., and M. Ortiz. Data-driven computing in dynamics. *Int. J. Numer. Meth. Engrg*. 113(11):1697–1710, 2018.
[19]Kulin, R.M., F. Jiang, and K.S. Vecchio. Effects of age and loading rate on equine cortical bone failure. *J. Mech. Behav. Biomed. Mater*. 4: 57–75, 2011.
[20]Ladeveze, P. The large time increment method for the analysis of structures with non-linear behavior described by internal variables. *CR Acad. Sci. Ser. II* 309(11):1095–1099, 1989.
[21]Larose, D.T. Discovering Knowledge in Data: An Introduction to Data Mining. John Wiley and Sons, 2014.
[22]Latorre, M., and F.J. Montans. What-you-prescribe-is-what-you-get orthotropic hyperelasticity. *Comput. Mech*. 53(6):1279–1298, 2014.
[23]Manyika, J., M. Chui, B. Brown, J. Bughin, R. Dobbs, C. Roxburgh, and A.H. Byers. Big data: the next frontier for innovation, competition, and productivity. 2011.
[24]Mariappan, Y.K., K.J. Glaser, and R.L. Ehman. Magnetic resonance elastography: a review. *Clin. Anat*. 23:497–511, 2010.
[25]McKee, C.T., J.A. Last, P. Russell, and C.J. Murphy. Indentation versus tensile measurements of Young's modulus for soft biological tissues. *Tissue Eng*. 17: 155–164, 2011.
[26]Mora-Macías, J., A. Pajares, P. Miranda, J. Domínguez, and E. Reina-Romo. Mechanical characterization via nanoindentation of the woven bone developed during bone transport. *J. Mech. Behav. Biomed. Mater*. 74: 236–244, 2017.
[27]Pal, S. Design of Artificial Human Joints and Organs. Chapter 2: Mechanical Properties of Biological Materials. Springer, 2014.
[28]Raghupathi, W., and V. Raghupathi. Big data analytics in healthcare: promise and potential. *Health Inf. Sci. Sys*. 2(1):1, 2014.
[29]Reilly, G.C., and J.D. Currey. The development of microcracking and failure in bone depends on the loading mode to which it is adapted. *J. Exp. Biol*. 202:543–552, 1999.
[30]Rho, J.Y., J.D. Currey, P. Zioupos, and G.M. Pharr. The anisotropic Young's modulus of equine secondary osteones and interstitial bone determined by nanoindentation. *J. Exp. Biol*. 204:1775–1781, 2001.
[31]Riggs, C.M., L.C. Vaughan, G.P. Evans, L.E. Lanyon, and A. Boyde. Mechanical implications of collagen fibre orientation in cortical bone of the equine radius. *Anat. Embryol*. 187:239–248, 1993.
[32]Sacks, M. Biaxial mechanical evaluation of planar biological materials. *J. Elasticity* 61: 199–246, 2000.
[33]Sarvazyan, A.P., A.R. Skovoroda, S.Y. Emelianov, J.B. Fowlkes, J.G. Pipe, R.S. Adler, R.B. Buxton, and P.L. Carson. Biophysical Bases of Elasticity Imaging. In: Jones JP, editor. Acoustical Imaging. NewYork: Plenum Press. 223–240, 1995.
[34]Schryver, H.F. Bending properties of cortical bone of the horse. *Am. J. Vet. Res*. 3925–3928, 1978.
[35]Skalak, R., and S. Chien. Handbook of Bioengineering. , McGraw-Hill, 1987.
[36]Sutton, M.A., S.R. McNeill, J.D. Helm, and Y.J. Chao. Advances in two-dimensional and three-dimensional computer vision. In: Rastogi PK, editor. Photomechanics, Topics Appl. Phys. Springer-Verlag Berlin Heidelberg 2000, 77, 323–372, 2000.
[37]Sutton, M.A., J.J. Orteu, and H. Schreier. Digital Image Correlation (Chapter 5), In: Sutton M.A., Orteu J.J. and Schreier H., Image Correlation for Shape, Motion and Deformation Measurements: basic concepts theory and applications, pp. 81–116, 2009.
[38]Tai, K., M. Dao, S. Suresh, A. Palazoglu, and C. Ortiz. Nanoscale heterogeneity promotes energy dissipation in bone. *Nat. Mater*. 6:454–462, 2007.
[39]Taylor, W.R., E. Roland, H. Ploeg, D. Hertig, R. Klabunde, M.D. Warner, M.C. Hobatho, L. Rakotomanana, and S.E. Clift. Determination of orthotropic bone elastic constants using FEA and modal analysis. *J. Biomech*. 35:767–773, 2002.
[40]Thompson, M.S., H. Schell, J. Lienau, and G.N. Duda. Digital image correlation: A technique for determining local mechanical conditions within early bone callus. *Med. Eng. Phys*. 29:820–823, 2007.
[41]Vázquez, J. Efecto de las Tensiones Residuales en la Fatiga por Fretting. PhD Thesis. University of Seville, 2010.
[42]Zienkiewicz, O.C., and R.L. Taylor. The Finite Element Method, fifth edition. Butterworth–Heinemann, Oxford, 2000.